ACS OMEGA

http://pubs.acs.org/journal/acsodf

Article

Observation of Exchange Bias in Antiferromagnetic $Cr_{0.79}Se$ Due to the Coexistence of Itinerant Weak Ferromagnetism at Low Temperatures

Sayan Routh and Setti Thirupathaiah*

Cite This: *ACS Omega* 2021, 6, 28012−28018

Read Online

ACCESS | Metrics & More | Article Recommendations

ABSTRACT: We report on the structural, electrical transport, and magnetic properties of antiferromagnetic transition-metal monochalcogenide $Cr_{0.79}Se$. Different from the existing off-stoichiometric compositions, $Cr_{0.79}Se$ is found to be synthesized into the same NiAs-type hexagonal crystal structure as that of CrSe. Resistivity data suggest $Cr_{0.79}Se$ to be a Fermi-liquid-type metal at low temperatures, while at intermediate temperatures, the resistivity depends sublinearly on the temperature. Eventually, at elevated temperatures, the rate of change of resistivity rapidly decreases with increasing temperature. Magnetic measurements suggest a transition from the paramagnetic phase to an antiferromagnetic phase at a Néel temperature of 225 K. Further reduction of the sample temperature results in the coexistence of weak ferromagnetism along with the antiferromagnetic phase below 100 K. As a result, below 100 K, we identify a significant exchange bias due to the interaction between the ferro- and antiferromagnetic phases. In addition, from temperature-dependent X-ray diffraction measurements, we observe that the NiAs-type structure is stable up to as high as 600 °C.

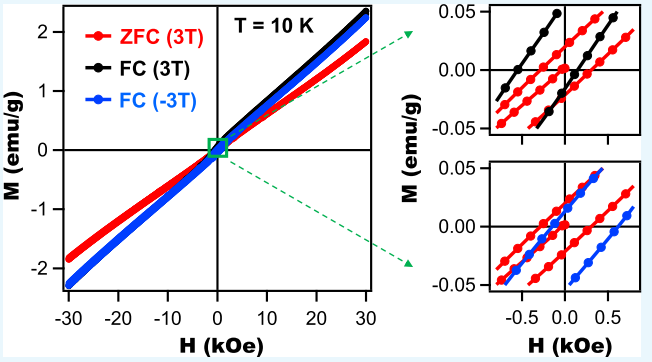

INTRODUCTION

The design and synthesis of materials with a strong magnetic exchange bias (EB) property has been one of the intense research activities for the past several decades[1] and till date[2−5] due to materials' potential applications in spintronic devices.[6,7] There exist several studies on designing multilayered and core−shell structures to generate an effective large exchange bias at the interface of a ferromagnetic (FM) and an antiferromagnetic (AFM) layer.[8−12] Several bulk materials too have been synthesized, showing large exchange bias.[13−15] But most of the bulk materials are in the form of nanocomposites or with a complicated crystal structure of the doped ternary compounds. In this paper, we discuss the exchange bias in a transition-metal monochalcogenide having the simplest crystal structure.

Transition-metal monochalcogenides with the chemical formula of MX (M = Fe, Cr; X = S, Se, Te) are versatile materials due to their diverse structural, electronic, and magnetic properties. For instance, Fe_xSe is a nonmagnetic high-temperature superconductor with a T_c of 8 K and a tetragonal crystal structure for $x \geq 1$,[16] while it is an antiferromagnetic metal with a hexagonal crystal structure for $x < 1$.[17] However, FeTe is always a tetragonal antiferromagnetic system with a stripe order.[18,19] Further, FeS is found to be a nonmagnetic superconductor with a tetragonal crystal structure.[20] On the other hand, similar to Fe_xX, Cr_xX (X = S, Se, Te) systems too are diverse in their structural, electronic, and magnetic properties.[21−26] For instance, Cr_xTe is a ferromagnetic half-metal and can exist in any zinc blend (ZB),[27] rock salt (RS),[28] or NiAs[29] crystal structure type, whereas Cr_xS[30] and Cr_xSe[31] are mostly known for their antiferromagnetic nature with the NiAs-type crystal structure. Some reports suggested Cr_xSe to be a spin-glass-type magnetic system[32] and Cr_xS to be a ferrimagnetic metal.[33]

In this paper, we report a comprehensive study on the structural, electrical transport, and magnetic properties of $Cr_{0.79}Se$ in the polycrystal form. To date, not many experimental studies are available on this system despite it being a noncollinear AFM metal.[31] Recently, it was suggested that antiferromagnetic metals with noncollinear spin texture are promising candidates for the anomalous Hall effect, induced by the berry curvature.[34−36] Motivated by this, we reinvestigated the structural, electrical, magnetic properties of

Received: July 26, 2021
Accepted: September 30, 2021
Published: October 11, 2021

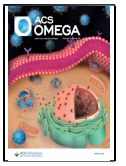

this system. Our X-ray diffraction (XRD) studies demonstrate that $Cr_{0.79}Se$ has a NiAs-type structure. At higher temperatures, we noticed a shift in certain XRD peak positions, leading to a change in lattice parameters with temperature. In addition, from the XRD measurements, we observe that the NiAs-type structure is stable up to as high as a 600 °C sample temperature. Electrical resistivity studies show Fermi-liquid-like metallic behavior at low temperatures (<41 K), and in the intermediate temperature ranges (41−200 K), the resistivity changes sublinearly with temperature. Further, at elevated temperatures (>200 K), the rate of change of resistivity rapidly decreases with temperature. Magnetic property studies suggest a transition from the paramagnetic phase to an antiferromagnetic phase at a Néel temperature of 225 K. Further, below 100 K, weak ferromagnetism is found, which coexists with antiferromagnetism.

RESULTS

Figure 1a shows Rietveld refinement on the XRD data of $Cr_{0.79}Se$ measured at room temperature (RT). It is evident from the XRD data that $Cr_{0.79}Se$ crystallizes into the NiAs-type crystal structure with a hexagonal space group of $P6_3/mmc$(194). The estimated lattice parameters from the Rietveld refinement are found to be $a = b = 3.6811(3)$ Å and $c = 6.0198(6)$ Å. No additional impurity peaks were noticed from the XRD data, demonstrating a high phase purity of the sample. Further, we performed XRD measurements as a function of temperature starting from RT to 600 °C, as shown in Figure 2a. From the temperature-dependent XRD data, we noticed that the peak positions are relatively shifted with temperature. To demonstrate the peak shift, in Figure 2b, we fixed a peak position of reflection $(1\bar{1}1)$ to notice a significant shift in the peak position of reflection $(01\bar{3})$. To elucidate the structural changes with temperature, we performed Rietveld refinement for the XRD data at each measured temperature. The obtained lattice parameters are plotted as a function of temperature as shown in Figure 2c. We identify that the lattice parameter $a(b)$ is almost constant, changing from 3.681 to 3.712 Å, while the lattice parameter c substantially increases from 6.024 to 6.113 Å in going from RT to 600 °C. Consequently, the unit cell volume also increases with temperature as shown in Figure 2d.

Figure 3 shows the temperature-dependent electrical resistivity of $Cr_{0.79}Se$ measured within the temperature range of 3.1−310 K. We observe from the resistivity data that at low temperatures (T < 41 K), the data fits well with the Fermi-liquid law of resistivity ($\propto aT^2$). But beyond 41 K, the data follows a sublinear behavior ($\propto bT^{0.62}$) with temperature up to 200 K. The inset in Figure 3 confirms the Fermi-liquid nature of resistivity, as we notice a perfect linear relation between ρ and T^2 (for T up to 41 K). The bottom panel of Figure 3 presents the plot of $d\rho/dT$ vs T. We notice that $d\rho/dT$ increases with T up to 41 K, above 41 K, $d\rho/dT$ decreases with T up to 302 K, and beyond 302 K, $-d\rho/dT$ decreases with T, hinting at an electronic phase transition at this temperature as

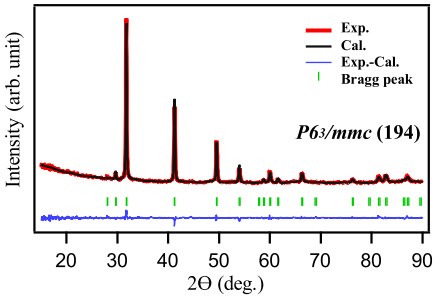

Figure 1. Powder X-ray diffraction pattern and Rietveld refinement of $Cr_{0.79}Se$, confirming the NiAs-type crystal structure with a space group of $P6_3/mmc$ (194).

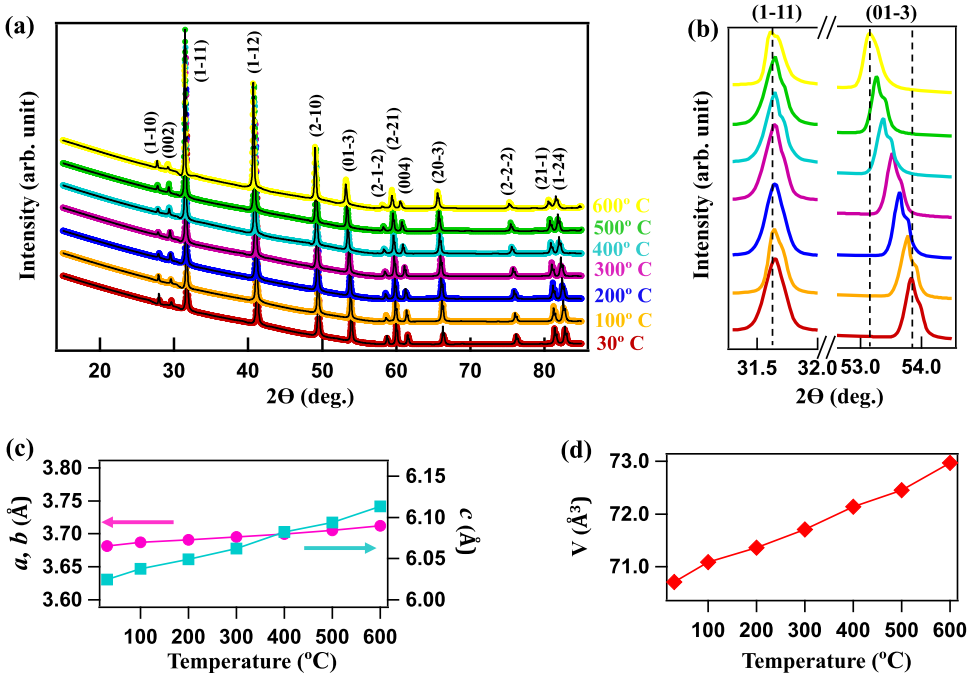

Figure 2. (a) Temperature-dependent powder X-ray diffraction pattern of $Cr_{0.79}Se$ overlapped with Rietveld refinement. (b) Enlarged XRD patterns for the reflections of $(1\bar{1}1)$ and $(01\bar{3})$. (c) Plot of lattice constants a, b, and c as a function of temperature. (d) Plot of cell volume (V) as a function of temperature.

https://doi.org/10.1021/acsomega.1c03986
ACS Omega 2021, 6, 28012−28018

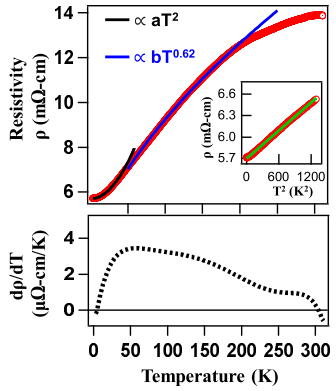

Figure 3. Temperature-dependent electrical resistivity of $Cr_{0.79}Se$. A black solid curve represents T^2 law fitting up to 41 K and the blue solid curve represents sublinear fitting between 41 and 200 K. The inset shows the plot of ρ *vs* T^2. The green line in the inset is a linear fit to the data. The bottom image represents $d\rho/dT$ *vs* T.

$d\rho/dT$ becomes negative. Next, in Figure 4, we show magnetization (M) as a function of temperature measured

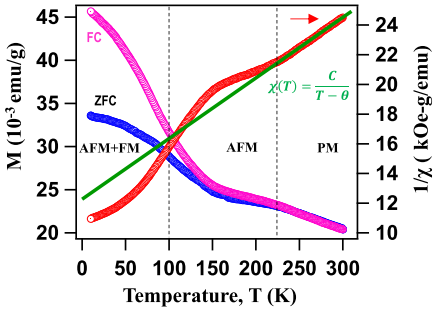

Figure 4. Magnetization as a function of temperature plotted for zero-field-cooled (ZFC) and field-cooled (FC) modes. Susceptibility as a function of temperature is plotted for the FC mode. The green curve is a susceptibility fitting with the Curie–Weiss law.

under zero-field-cooled (ZFC) and field-cooled (FC) modes at an applied external magnetic field of 500 Oe. In Figure 4, we further show inverse magnetic susceptibility ($1/\chi$) as a function of temperature measured in the FC mode. As can be seen from Figure 4, at higher temperatures (T > 225 K), susceptibility follows the Curie–Weiss law

$$\chi(T) = \frac{C}{T - \Theta} \tag{1}$$

where C is the Curie constant and Θ is the Curie–Weiss temperature. From the fitting, we found a Curie–Weiss temperature of $\Theta = -300 \pm 2$ K and a Curie constant of $C = 24.5 \pm 0.5$ Oe·gm·emu^{-1}·K^{-1}. The negative Curie–Weiss temperature suggests dominant antiferromagnetic interactions in the system. We further calculated the effective magnetic moment of Cr ion in the paramagnetic regime using the formula $\mu_{eff} = 2.84\sqrt{MC}\,\mu_B = 5.08\mu_B$/Cr.[37] In addition, we observe a deviation from the linear dependence of $1/\chi$ on T below 225 K, suggesting a magnetic transition from a paramagnetic to an antiferromagnetic phase.

Figure 5 depicts M–H curves taken in the ZFC mode with an applied magnetic field of 1.5 T at temperatures 10, 100, and 150 K. From the inset shown at the bottom of Figure 5, we observe hysteresis in the M–H loop with a coercive field of H_c

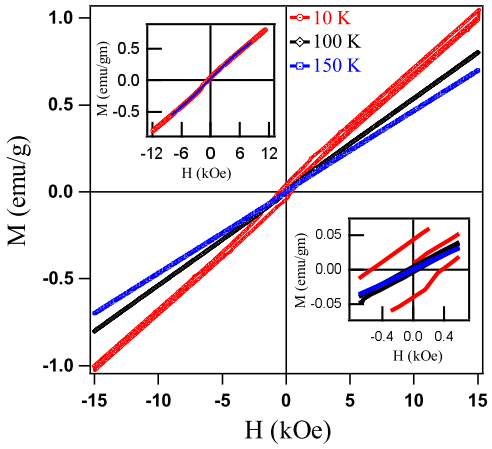

Figure 5. Magnetization (M) as a function of the applied magnetic field (H) is plotted for the ZFC mode at sample temperatures of 10, 100, and 150 K. The top-left inset shows M–H curve fit using eq 2. The bottom-right inset shows enlarged data around the zero magnetic field to show the hysteresis of the M–H curve at 10 K, which disappears above 100 K.

= 410 Oe when measured at 10 K, and it disappears at 100 K. The presence of hysteresis loops suggests a ferromagnetic order at low temperatures. Also, magnetization saturation is not reached up to the applied field of 1.5 T, suggesting a strong AFM order as well in this system. To quantify the strength of ferromagnetism in the system, as shown in the top-left inset of Figure 5, we performed M–H curve fitting with eq 2[38] to estimate the saturation magnetization $M_s = 1.3 \pm 0.1$ emu/g and remanent magnetization $M_r = 0.09 \pm 0.01$ emu/g, while having the experimental coercive field H_c = 410 Oe and susceptibility $\chi = 9.1 \times 10^{-5}$ emu/(Oe g). These values suggest weak ferromagnetism in $Cr_{0.79}Se$.

$$M(H) = \frac{2M_s}{\pi}\tan^{-1}\left[\left(\frac{H}{H_c}\pm 1\right)\tan\left(\frac{\pi M_r}{2M_s}\right)\right] + \chi H \tag{2}$$

Figure 6a depicts M–H curves measured in the FC mode at various sample temperatures using the applied magnetic field of 3 T. The inset at the bottom-right of Figure 6a demonstrates a significant shift in the M–H loop hysteresis, hinting at the presence of exchange bias in this sample. Figure 6b depicts M–H curves in the FC mode at a fixed sample temperature of 10 K by varying the applied magnetic fields: 3, 6, and 9 T. The bottom-right inset of Figure 6b is the zoomed-in image of M–H loops in which we notice hysteresis at all applied magnetic fields. Further, the bottom-left inset of Figure 6b is the zoomed-in image of the M–H loop measured with a magnetic field of 9 T, demonstrating the presence of hysteresis between 6 and 9 T. Figure 6c depicts the exchange bias (H_{EB}) and coercivity (H_c) plotted as a function of temperature. From Figure 6c, we observe that both H_{EB} and H_c decrease with an increase in temperature and become negligible above 100 K within an instrumental error of ±20 Oe. Figure 6d depicts the training effect on the exchange bias. We observe a significant decrease (15%) in the exchange bias after repeating four cycles of M–H loops. The observation of exchange bias under the FC mode but not under the ZFC mode is in line with the phenomenon of the exchange bias, as explained for various magnetic alloys and compounds.[39]

https://doi.org/10.1021/acsomega.1c03986
ACS Omega 2021, 6, 28012–28018

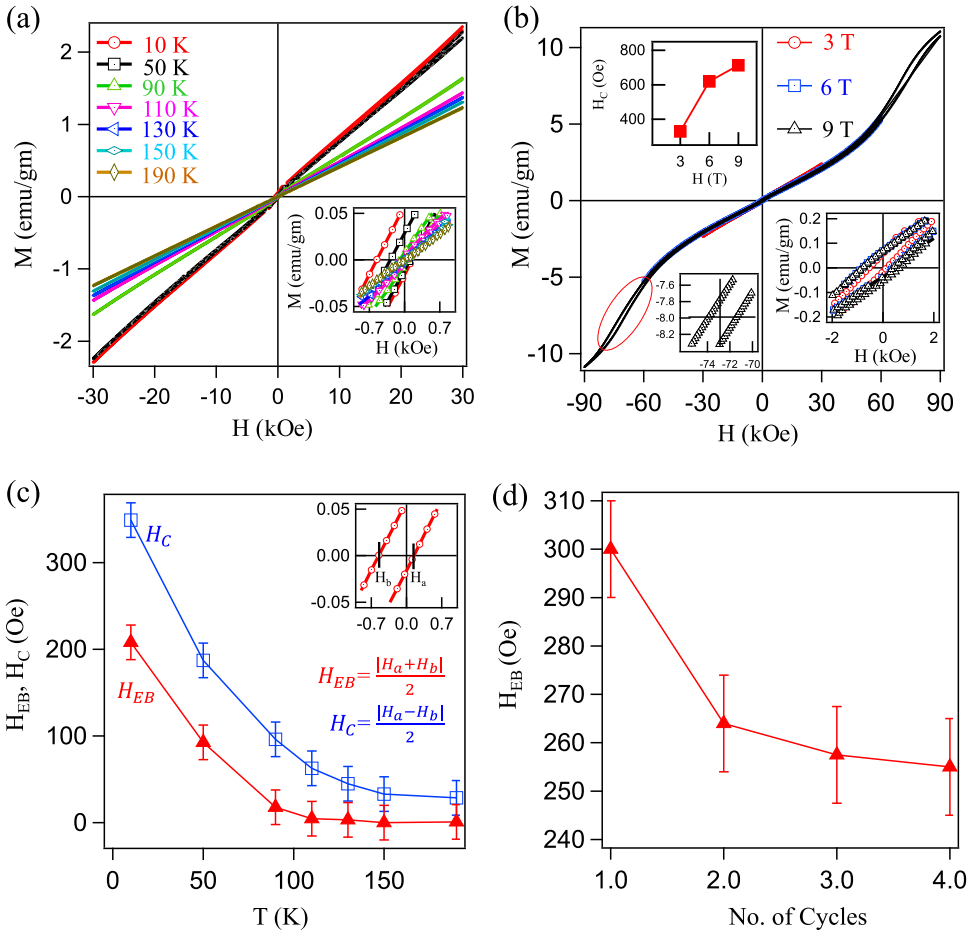

Figure 6. (a) $M-H$ loops plotted for the FC mode at various sample temperatures. The inset in (a) is enlarged data around the zero magnetic field to show the hysteresis of the $M-H$ curve. (b) $M-H$ curves plotted for the FC mode at various applied magnetic fields. The bottom-right inset in (b) is enlarged data around the zero magnetic field to show the hysteresis of the $M-H$ curve at various applied fields. The bottom-left inset in (b) is enlarged data to show the hysteresis of the $M-H$ curve for the applied field of 9 T. The top-left inset in (b) shows the coercive field as a function of the applied field. (c) Exchange bias (H_{EB}) and coercive field (H_c) are plotted as a function of temperature measured with a 3 T magnetic field in the FC mode. (d) Plot of H_{EB} *vs* number of $M-H$ loop cycles.

DISCUSSION

The studied sample, $Cr_{0.79}Se$, has been found to have the NiAs-type structure of the hexagonal crystal symmetry as demonstrated in Figures 1 and 2, which is consistent with the crystal structure of stoichiometric CrSe.[40] On the other hand, the crystal symmetry of the existing off-stoichiometric systems of Cr_xSe deviates from the stoichiometric system. For instance, $Cr_{0.67}Se$ possesses a trigonal crystal symmetry with a space group of $R\bar{3}H$ (148),[41] while $Cr_{0.875}Se$, $Cr_{0.75}Se$, and $Cr_{0.625}Se$ possess the monoclinic crystal symmetry with a space group of $C1_2/m1$ (12).[42−44] Most importantly, we identify that $Cr_{0.79}Se$ is the first-known off-stoichiometric composition crystallizing in the $P6_3/mmc$ space group. Further, from the temperature-dependent XRD data, we notice peak shifting with temperature. Such a peak position shift with temperature generally leads to a change in the lattice parameters while still preserving the crystal symmetry. This is supported by the Rietveld refinement (see Figure 2). Thus, our studies confirm that the NiAs crystal structure of $Cr_{0.79}Se$ is stable up to 600 °C from room temperature. Though Jahn−Teller distortion has not been observed so far in any of the off-stoichiometric Cr_xSe compositions, in the case of stoichiometric CrSe, it has been suggested for temperatures below 305 °C.[45] However, we do not observe any signature of Jahn−Teller distortion from our temperature-dependent XRD data in the studied compound.

Next, from the electrical resistivity data shown in Figure 3a it is clear that $Cr_{0.79}Se$ is a Fermi-liquid-type metal below 41 K. But above 41 K, the system deviates to a non-Fermi-liquid type metal showing a sublinear dependence of resistivity on temperature up to 200 K. The same is confirmed from the $d\rho/dT$ *vs* T curve [see the bottom of Figure 3a]. From this curve, we observe that $d\rho/dT$ increases with temperature up to 41 K and then, it decreases with T to reach zero at 302 K. Above 302 K, $-d\rho/dT$ decreases with increasing T up to the measured temperature of 310 K. This observation hints at a metal−insulator (MI) transition above 302 K in $Cr_{0.79}Se$. MI transition has been noticed in some of the other transition-metal monochalcogenides as well. For instance, in $Fe_{0.875}Se$, MI transition is observed at 100 K due to a proximity effect of magnetic moment reorientation.[17] Note here that similar kind of resistivity data have been reported earlier in the case of $Cr_{0.67}Se$ single crystals[46] with a sublinear behavior of resistivity up to 175 K and then changing resistivity slope above this temperature. But note that the antiferromagnetic ordering in $Cr_{0.67}Se$ is found only below 60 K, while in our sample, the antiferromagnetic ordering is found at 225 K. Another report on $Cr_{0.68}Se$ single crystals also suggested an antiferromagnetic

https://doi.org/10.1021/acsomega.1c03986
ACS Omega 2021, 6, 28012−28018

ordering below 42 K, but unlike $Cr_{0.67}Se$, which is metal up to 300 K, $Cr_{0.68}Se$ is found to be a small-gap semiconductor (E_g = 3.9 meV)[35] down to the lowest possible measured temperature. Thus, the electrical properties of Cr_xSe systems seem to be highly sensitive to Cr atom concentration, which may directly affect the charge carrier density near the Fermi level and the disorder of the system rather than the magnetic interactions as we do not find any one−one correlation between the magnetic transition temperatures (see Figures 4−6) and the temperature-dependent resistivity (see Figure 3).

Finally, regarding the important observations of this study, we found weak ferromagnetism in $Cr_{0.79}Se$ below T_c = 100 K that coexisted with the AFM phase. As a result, an exchange bias was observed in this system below T_c. Usually, CrSe is known for its noncollinear AFM phase. But recently, one report showed weak ferromagnetism in $Cr_{0.67}Se$ along with the AFM phase below 50 K.[46] However, not much discussion has been carried out on the presence of the exchange bias in $Cr_{0.67}Se$. Thus, we report the exchange bias for the first time in these systems. Another report on neutron diffraction studies of $Cr_{0.67}Se$ suggested two magnetic phases, a noncollinear AFM phase at a low temperature (<38 K) and a collinear AFM phase at a high temperature (38 > T < 45 K), but it did not find ferromagnetism at as low as 6 K.[41] On the other hand, the estimated effective paramagnetic moment of 5.08μ_B/Cr in our systems is slightly higher than the effective paramagnetic moment of 4.5μ_B/Cr in the stoichiometric CrSe.[29] This could be mostly because of the mixed Cr valance states in the off-stoichiometric compositions.[47,48] Although earlier a spin-glass-like magnetic phase has been observed due to the frustrated magnetic moments between the AFM and FM phases,[32] in our system, from the M−T data (see Figure 4), we do not see any sign of the spin-glass-like behavior below T_c.

CONCLUSIONS

In summary, we systematically studied the structural, electrical transport, and magnetic properties of the antiferromagnetic transition-metal monochalcogenide $Cr_{0.79}Se$. We identify that $Cr_{0.79}Se$ is synthesized into the same NiAs-type hexagonal crystal structure as that of the stoichiometric CrSe, unlike the other off-stoichiometric systems that form in differing crystal symmetries. Resistivity data suggest $Cr_{0.79}Se$ to be a Fermi-liquid-type metal at low temperatures, while at higher temperatures, the resistivity depends sublinearly on temperature. Above room temperature, the resistivity data hints at a MI transition, but we need more studies to confirm the same. Magnetic measurements suggest a transition from the paramagnetic phase to an antiferromagnetic phase at a Néel temperature of 225 K. Importantly, weak ferromagnetism is noticed below 100 K along with antiferromagnetism. As a result, we notice significant exchange bias below 100 K due to the interaction between the ferro- and antiferromagnetic phases.

METHODS

Samples of $Cr_{0.79}Se$ are prepared by the standard solid-state reaction method[40] by mixing high-purity powders of chromium (4 N, Alfa Aesar) and selenium (5 N, Alfa Aesar) elements in an appropriate ratio. The well-mixed powders were then heated in a muffle furnace at 1000 °C for 48 h. The final sample was pressed into a pellet form and heated again at 1000 °C for another 48 h. The as-prepared polycrystalline sample was structurally characterized using a powder X-ray diffractometer (XRD) equipped with Cu Kα radiation (Rigaku-SmartLab) (9 kW) at various sample temperatures (30−600 °C). Rietveld refinement analysis of the XRD data was performed using the FULLPROF software package.[49] Energy-dispersive X-ray (EDX) analysis suggests the chemical composition of the as-prepared sample to be $Cr_{0.79}Se$. Electrical resistivity measurements were carried out using the standard four-probe technique with a closed-cycle refrigerator (CCR)-based cryostat, within a temperature range of 3.1−310 K. Conducting silver epoxy and Cu wires were used to make the electrical contacts. Magnetic property measurements were carried out using a vibrating sample magnetometer (VSM) (DynaCool, Quantum Design) up to a magnetic field of 9 T.

AUTHOR INFORMATION

Corresponding Author

Setti Thirupathaiah − *Department of Condensed Matter Physics and Material Sciences, S N Bose National Centre for Basic Sciences, Kolkata, West Bengal 700106, India;* orcid.org/0000-0003-1258-0981; Email: setti@bose.res.in

Author

Sayan Routh − *Department of Condensed Matter Physics and Material Sciences, S N Bose National Centre for Basic Sciences, Kolkata, West Bengal 700106, India*

Complete contact information is available at: https://pubs.acs.org/10.1021/acsomega.1c03986

Notes

The authors declare no competing financial interest.

ACKNOWLEDGMENTS

S.T. acknowledges the financial support given by SNBNCBS through the Faculty Seed Grants program. The authors thank the Science and Engineering Research Board (SERB), Department of Science and Technology (DST), India, for the financial support through start-up research grants (SRG/2020/000393).

REFERENCES

(1) Meiklejohn, W. H.; Bean, C. P. New Magnetic Anisotropy. *Phys. Rev.* **1957**, *105*, 904−913.

(2) Wang, B. M.; Liu, Y.; Ren, P.; Xia, B.; Ruan, K. B.; Yi, J. B.; Ding, J.; Li, X. G.; Wang, L. Large Exchange Bias after Zero-Field Cooling from an Unmagnetized State. *Phys. Rev. Lett.* **2011**, *106*, No. 077203.

(3) Nayak, A. K.; Nicklas, M.; Chadov, S.; Khuntia, P.; Shekhar, C.; Kalache, A.; Baenitz, M.; Skourski, Y.; Guduru, V. K.; Puri, A.; Zeitler, U.; Coey, J. M. D.; Felser, C. Design of compensated ferrimagnetic Heusler alloys for giant tunable exchange bias. *Nat. Mater.* **2015**, *14*, 679−684.

(4) Saha, A.; Sohoni, S.; Viswanatha, R. Interface Modeling Leading to Giant Exchange Bias from the $CoO/CoFe_2O_4$ Quantum Dot Heterostructure. *J. Phys. Chem. C* **2019**, *123*, 2421−2427.

(5) Tian, F.; Li, Y.; Zhao, Q.; Fang, M.; Zhang, R.; Dai, Z.; Yu, Z.; Ke, X.; Zhang, Y.; Zhou, C.; Yang, S. Maximizing Zero-Field-Cooled Exchange Bias in Crystallized Co@CoO Nanocluster Assembled Thin Film by Varying Film Thickness. *J. Phys. Chem. C* **2021**, *125*, 7337−7342.

(6) Parkin, S. Spintronic materials and devices: past, present and future. In *IEDM Technical Digest. IEEE International Electron Devices Meeting*, 2004; pp 903−906.

(7) Hirohata, A.; Takanashi, K. Future perspectives for spintronic devices. *J. Phys. D: Appl. Phys.* **2014**, *47*, No. 193001.

(8) Inderhees, S. E.; Borchers, J. A.; Green, K. S.; Kim, M. S.; Sun, K.; Strycker, G. L.; Aronson, M. C. Manipulating the Magnetic Structure of Co Core/CoO Shell Nanoparticles: Implications for Controlling the Exchange Bias. *Phys. Rev. Lett.* **2008**, *101*, No. 117202.
(9) Lage, E.; Kirchhof, C.; Hrkac, V.; Kienle, L.; Jahns, R.; Knöchel, R.; Quandt, E.; Meyners, D. Exchange biasing of magnetoelectric composites. *Nat. Mater.* **2012**, *11*, 523−529.
(10) Lavorato, G. C.; Winkler, E. L.; Lima, E.; Zysler, R. D. *Exchange Bias*; CRC Press, 2017; pp 47−70.
(11) Perzanowski, M.; Krupinski, M.; Zarzycki, A.; Dziedzic, A.; Zabila, Y.; Marszalek, M. Exchange Bias in the $[CoO/Co/Pd]_{10}$ Antidot Large Area Arrays. *ACS Appl. Mater. Interfaces* **2017**, *9*, 33250−33256.
(12) Song, N.; Yang, H.; Luo, Y.; Ren, X.; Zhou, J.; Geng, S.; Zhao, G.; Zhang, X.; Cheng, Z. Well-controlled exchange bias effect in $MnO@Mn_3O_4$ core-shell nanoparticles with an inverted coupling structures. *AIP Adv.* **2017**, *7*, No. 045316.
(13) Wisniewski, A.; Fita, I.; Puzniak, R.; Markovich, V. *Exchange Bias*; CRC Press, 2017; pp 275−299.
(14) Belik, A. A. Origin of Magnetization Reversal and Exchange Bias Phenomena in Solid Solutions of $BiFeO_3$−$BiMnO_3$: Intrinsic or Extrinsic. *Inorg. Chem.* **2013**, *52*, 2015−2021.
(15) Fertman, E. L.; Fedorchenko, A. V.; Desnenko, V. A.; Shvartsman, V. V.; Lupascu, D. C.; Salamon, S.; Wende, H.; Vaisburd, A. I.; Stanulis, A.; Ramanauskas, R.; Olekhnovich, N. M.; Pushkarev, A. V.; Radyush, Y. V.; Khalyavin, D. D.; Salak, A. N. Exchange bias effect in bulk multiferroic $BiFe_{0.5}Sc_{0.5}O_3$. *AIP Adv.* **2020**, *10*, No. 045102.
(16) Hsu, F.-C.; Luo, J.-Y.; Yeh, K.-W.; Chen, T.-K.; Huang, T.-W.; Wu, P. M.; Lee, Y.-C.; Huang, Y.-L.; Chu, Y.-Y.; Yan, D.-C.; Wu, M.-K. Superconductivity in the PbO type structure FeSe. *Proc. Natl. Acad. Sci.* **2008**, *105*, 14262−14264.
(17) Li, G.; Zhang, B.; Baluyan, T.; Rao, J.; Wu, J.; Novakova, A. A.; Rudolf, P.; Blake, G. R.; de Groot, R. A.; Palstra, T. T. M. Metal−Insulator Transition Induced by Spin Reorientation in Fe_7Se_8 Grain Boundaries. *Inorg. Chem.* **2016**, *55*, 12912−12922.
(18) Maheshwari, P. K.; Jha, R.; Gahtori, B.; Awana, V. P. S. Structural and Magnetic Properties of Flux-Free Large FeTe Single Crystal. *J. Supercond. Novel Magn.* **2015**, *28*, 2893−2897.
(19) Hänke, T.; Singh, U. R.; Cornils, L.; Manna, S.; Kamlapure, A.; Bremholm, M.; Hedegaard, E. M. J.; Iversen, B. B.; Hofmann, P.; Hu, J.; Mao, Z.; Wiebe, J.; Wiesendanger, R. Reorientation of the diagonal double-stripe spin structure at Fe_yTe bulk and thin-film surfaces. *Nat. Commun.* **2017**, *8*, No. 13939.
(20) Zhang, J.; Liu, F.-L.; Ying, T.-P.; Li, N.-N.; Xu, Y.; He, L.-P.; Hong, X.-C.; Yu, Y.-J.; Wang, M.-X.; Shen, J.; Yang, W.-G.; Li, S.-Y. Observation of two superconducting domes under pressure in tetragonal FeS. *npj Quant. Mater.* **2017**, *2*, No. 49.
(21) Chen, J.; Wang, L.; Zhang, M.; Zhou, L.; Zhang, R.; Jin, L.; Wang, X.; Qin, H.; Qiu, Y.; Mei, J.; Ye, F.; Xi, B.; He, H.; Li, B.; Wang, G. Evidence for Magnetic Skyrmions at the Interface of Ferromagnet/Topological-Insulator Heterostructures. *Nano Lett.* **2019**, *19*, 6144−6151.
(22) Yang, W.; Coughlin, A. L.; Webster, L.; Ye, G.; Lopez, K.; Fertig, H. A.; He, R.; Yan, J.-A.; Zhang, S. Highly tunable Raman scattering and transport in layered magnetic Cr_2S_3 nanoplates grown by sulfurization. *2D Mater.* **2019**, *6*, No. 035029.
(23) Li, H.; Wang, L.; Chen, J.; Yu, T.; Zhou, L.; Qiu, Y.; He, H.; Ye, F.; Sou, I. K.; Wang, G. Molecular Beam Epitaxy Grown Cr_2Te_3 Thin Films with Tunable Curie Temperatures for Spintronic Devices. *ACS Appl. Nano Mater.* **2019**, *2*, 6809−6817.
(24) Sun, X.; Li, W.; Wang, X.; Sui, Q.; Zhang, T.; Wang, Z.; Liu, L.; Li, D.; Feng, S.; Zhong, S.; et al. Room temperature ferromagnetism in ultra-thin van der Waals crystals of 1T-$CrTe_2$. *Nano Res.* **2020**, *13*, 3358−3363.
(25) Coughlin, A. L.; Xie, D.; Yao, Y.; Zhan, X.; Chen, Q.; Hewa-Walpitage, H.; Zhang, X.; Guo, H.; Zhou, H.; Lou, J.; Wang, J.; Li, Y. S.; Fertig, H. A.; Zhang, S. Near Degeneracy of Magnetic Phases in Two-Dimensional Chromium Telluride with Enhanced Perpendicular Magnetic Anisotropy. *ACS Nano* **2020**, *14*, 15256−15266.
(26) Huang, M.; Wang, S.; Wang, Z.; Liu, P.; Xiang, J.; Feng, C.; Wang, X.; Zhang, Z.; Wen, Z.; Xu, H.; et al. Colossal Anomalous Hall Effect in Ferromagnetic van der Waals $CrTe_2$. *ACS Nano* **2021**, *15*, 9759−9763.
(27) Sanyal, B.; Bergqvist, L.; Eriksson, O. Ferromagnetic materials in the zinc-blende structure. *Phys. Rev. B* **2003**, *68*, No. 054417.
(28) Liu, Y.; Bose, S. K.; Kudrnovský, J. First-principles theoretical studies of half-metallic ferromagnetism in CrTe. *Phys. Rev. B* **2010**, *82*, No. 094435.
(29) Lotgering, F.; Gorter, E. Solid solutions between ferromagnetic and antiferromagnetic compounds with NiAs structure. *J. Phys. Chem. Solids* **1957**, *3*, 238−249.
(30) Kamigaichi, T.; ichi Masumoto, K.; Hihara, T. Electrical Properties of Chromium Sulfides. *J. Phys. Soc. Jpn.* **1960**, *15*, 1355.
(31) Corliss, L. M.; Elliott, N.; Hastings, J. M.; Sass, R. L. Magnetic Structure of Chromium Selenide. *Phys. Rev.* **1961**, *122*, 1402−1406.
(32) Li, Y. B.; Zhang, Y. Q.; Li, W. F.; Li, D.; Li, J.; Zhang, Z. D. Spin-glass-like behavior and electrical transport properties of $Cr_7(Se_{1-x}Te_x)_8$. *Phys. Rev. B* **2006**, *73*, No. 212403.
(33) Konno, H.; Yuzuri, M. Ferrimagnetic Resonance on $CrS_{1.17}$. *J. Phys. Soc. Jpn.* **1988**, *57*, 621−625.
(34) Gan, L.-Y.; Zhang, Q.; Guo, C.-S.; Schwingenschlögl, U.; Zhao, Y. Two-Dimensional MnO_2/Graphene Interface: Half-Metallicity and Quantum Anomalous Hall State. *J. Phys. Chem. C* **2016**, *120*, 2119−2125.
(35) Yan, J.; Luo, X.; Chen, F. C.; Pei, Q. L.; Lin, G. T.; Han, Y. Y.; Hu, L.; Tong, P.; Song, W. H.; Zhu, X. B.; Sun, Y. P. Anomalous Hall effect in two-dimensional non-collinear antiferromagnetic semiconductor $Cr_{0.68}Se$. *Appl. Phys. Lett.* **2017**, *111*, No. 022401.
(36) Li, P.; Cai, T.-Y. Two-Dimensional Transition-Metal Oxides Mn_2O_3 Realized the Quantum Anomalous Hall Effect. *J. Phys. Chem. C* **2020**, *124*, 12705−12712.
(37) Makovetskii, G.; Shakhlevich, G. Magnetic properties of the $CrS_{1-x}Se_x$ system. *Phys. Status Solidi A* **1978**, *47*, 219−222.
(38) Patel, S. K. S.; Lee, J.-H.; Kim, M.-K.; Bhoi, B.; Kim, S.-K. Single-crystalline Gd-doped $BiFeO_3$ nanowires: R3c-to-Pn21a phase transition and enhancement in high-coercivity ferromagnetism. *J. Mater. Chem. C* **2018**, *6*, 526−534.
(39) Giri, S.; Patra; Majumdar, S. Exchange bias effect in alloys and compounds. *J. Phys.: Condens. Matter* **2011**, *23*, No. 073201.
(40) Tsubokawa, I. The Magnetic Properties of Chromium-Tellurium-Selenium System. *J. Phys. Soc. Jpn.* **1956**, *11*, 662−665.
(41) Adachi, Y.; Ohashi, M.; Kaneko, T.; Yuzuri, M.; Yamaguchi, Y.; Funahashi, S.; Morii, Y. Magnetic Structure of Rhombohedral Cr_2Se_3. *J. Phys. Soc. Jpn.* **1994**, *63*, 1548−1559.
(42) Chevreton, M.; Bertaut, E. Etude de seleniures de chrome. *C.R. Hebd. Seances Acad. Sci.* **1961**, *253*, 145.
(43) Blachnik, R.; Gunia, P.; Fischer, M.; Lutz, H. Das system chrom-selen. *J. Less-Common Met.* **1987**, *134*, 169−177.
(44) Sleight, A. W.; Bither, T. A. Chromium chalcogenides prepared at high pressure and the crystal growth of chromium sesquisulfide. *Inorg. Chem.* **1969**, *8*, 566−569.
(45) Masumoto, K.-i.; Hihara, T.; Kamigaichi, T. Anomalies in Electrical Conductivity and Magnetic Susceptibility of Chromium Selenides. *J. Phys. Soc. Jpn.* **1962**, *17*, 1209−1210.
(46) Wu, J.; Zhang, C.-L.; Yan, J.-M.; Chen, L.; Guo, L.; Chen, T.-W.; Gao, G.-Y.; Fei, L.; Zhao, W.; Chai, Y.; et al. Magnetotransport and magnetic properties of the layered noncollinear antiferromagnetic Cr_2Se_3 single crystals. *J. Phys.: Condens. Matter* **2020**, *32*, No. 475801.
(47) Andresen, A. F.; Zeppezauer, E.; Boive, T.; Nordström, B.; Brändén, C.-I. The Magnetic Structure of Cr_2Te_3, Cr_3Te_4, and Cr_5Te_6. *Acta Chem. Scand.* **1970**, *24*, 3495−3509.
(48) Liu, Y.; Petrovic, C. Critical behavior of the quasi-two-dimensional weak itinerant ferromagnet trigonal chromium telluride $Cr_{0.62}Te$. *Phys. Rev. B* **2017**, *96*, 134410.

https://doi.org/10.1021/acsomega.1c03986
ACS Omega 2021, 6, 28012−28018

(49) Rodríguez-Carvajal, J. Recent advances in magnetic structure determination by neutron powder diffraction. *Phys. B: Condens. Matter* **1993**, *192*, 55−69.

https://doi.org/10.1021/acsomega.1c03986
ACS Omega 2021, 6, 28012−28018